Bioactive Materials 39 (2024) 630–642

Contents lists available at ScienceDirect

Bioactive Materials

journal homepage: www.keaipublishing.com/en/journals/bioactive-materials

Smart responsive staple for dynamic promotion of anastomotic stoma healing

Qi Sun [a,b,1], Zifeng Yang [b,1], Ruijun Xu [a,b,1], Renjie Li [b], Yang Li [b], Feng Wang [b,c,*], Yong Li [a,b,**]

[a] School of Medicine, South China University of Technology, Guangzhou, Guangdong, 510006, China
[b] Department of Gastrointestinal Surgery, Department of General Surgery, Guangdong Provincial People's Hospital (Guangdong Academy of Medical Sciences), Southern Medical University, Guangzhou, 510080, China
[c] Guangxi Key Laboratory of Green Chemical Materials and Safety Technology, Guangxi Engineering Research Center for New Chemical Materials and Safety Technology, College of Petroleum and Chemical Engineering, Beibu Gulf University, Qinzhou, 535011, China

ARTICLE INFO

Keywords:
Anastomotic staple
Smart responsive
Coating
Tannic acid
Anastomotic stoma healing

ABSTRACT

The precise combination of conflicting biological properties through sophisticated structural and functional design to meet all the requirements of anastomotic healing is of great demand but remains challenging. Here, we develop a smart responsive anastomotic staple (Ti–OH-MC) by integrating porous titanium anastomotic staple with multifunctional polytannic acid/tannic acid coating. This design achieves dynamic sequential regulation of antibacterial, anti-inflammatory, and cell proliferation properties. During the inflammatory phase of the anastomotic stoma, our Ti–OH-MC can release tannic acid to provide antibacterial and anti-inflammatory properties, together with immune microenvironment regulation function. At the same time, as the healing progresses, the multifunctional coating gradually falls off to expose the porous structure of the titanium anastomotic staple, which promotes cell adhesion and proliferation during the later proliferative and remodeling phases. As a result, our Ti–OH-MC exceeds the properties of clinically used titanium anastomotic staple, and can effectively promote the healing. The staple's preparation strategy is simple and biocompatible, promising for industrialisation and clinical application. This work provides an effective anastomotic staple for anastomotic stoma healing and serve as a reference for the functional design and preparation of other types of titanium-based tissue repair materials.

1. Introduction

The precise coupling and sequential combination of antibacterial and anti-inflammatory properties with cell proliferation promotion, according to the microenvironment of different tissue repair phases, is of great demand for implantable tissue repair materials but remains challenging [1–5]. The titanium anastomotic staple commonly used in gastrointestinal surgery, can be considered as an ideal model to explore the biological applications of multifunctional implantable materials [6,7]. Anastomotic stoma healing is typically divided into three phases: the inflammatory phase, the proliferative phase, and the remodeling phase [8–10]. The inflammatory phase, lasting approximately 3–5 days, involves the secretion of large amounts of inflammatory factors and recruitment of immune cells to prevent the bacterial infection and remove the dead tissue. The inflammatory phase is susceptible to bacterial infection, which prolongs and exacerbates the inflammatory phase and negatively affects the healing process. The proliferative phase, occurring around 4–14 days post-anastomosis, is characterized by enhanced proliferation of fibroblasts and endothelial cells, increased formation of vessels, reduced tissue edema, and regenerated mucosal epithelium [11,12]. In the remodeling phase, collagen deposition and remodeling are crucial to improve anastomotic stoma strength. Given

Peer review under responsibility of KeAi Communications Co., Ltd.
* Corresponding author. Department of Gastrointestinal Surgery, Department of General Surgery, Guangdong Provincial People's Hospital (Guangdong Academy of Medical Sciences), Southern Medical University, Guangzhou, 510080, China.
** Corresponding author. School of Medicine, South China University of Technology, Guangzhou, Guangdong, 510006, China.
E-mail addresses: sunqi0831@163.com (Q. Sun), yangzifeng@gdph.org.cn (Z. Yang), xvruijun@163.com (R. Xu), renjieli120@outlook.com (R. Li), docliyang@126.com (Y. Li), wangfeng@gdph.org.cn (F. Wang), liyong@gdph.org.cn (Y. Li).
[1] These authors contributed equally: Qi Sun, Zifeng Yang and Ruijun Xu.

https://doi.org/10.1016/j.bioactmat.2024.04.021
Received 28 March 2024; Received in revised form 19 April 2024; Accepted 21 April 2024

the complicated nature of the digestive microenvironment, an ideal titanium anastomotic staple must cater to diverse biological requirements across different phases of the repair process [13,14]. During the inflammatory phase, the titanium anastomotic staple must exhibit potent antibacterial and anti-inflammatory properties while intelligently responding to the digestive microenvironment to regulate its antibacterial and anti-inflammatory levels. As the repair progresses to the proliferation and remodeling phases, which is dominated by cell proliferation, the titanium anastomotic staple should facilitate cell adhesion and tissue regeneration. However, conventional titanium anastomotic staple lacks these essential properties, is susceptible to bacterial colonization and cannot regulate the inflammatory environment, which is not conducive to anastomotic healing (Fig. 1a) [15]. Consequently, a significant disparity exists between conventional titanium anastomotic staple and the ideal anastomotic staple.

Recent studies have attempted to improve tissue repair by integrating antibacterial, anti-inflammatory, and cell-proliferating properties into titanium materials. However, these studies have mainly focused on addressing individual issues without providing comprehensive solutions. For example, antibacterial agents such as antibiotics, metal ions, metal oxides, and antimicrobial peptides are highly effective, but their use may inhibit cell proliferation and lead to drug resistance over time (Fig. 1b) [16–18]. Conversely, bioactive molecules such as miR-21, BMP-2, gelatin-CaPO, and MOFs, incorporated into titanium materials can promote cell proliferation but lack antibacterial and anti-inflammatory properties, which can lead to bacterial adhesion and proliferation during the early phases of tissue repair [19–21]. To resolve these shortcomings, studies have attempted to coat titanium materials

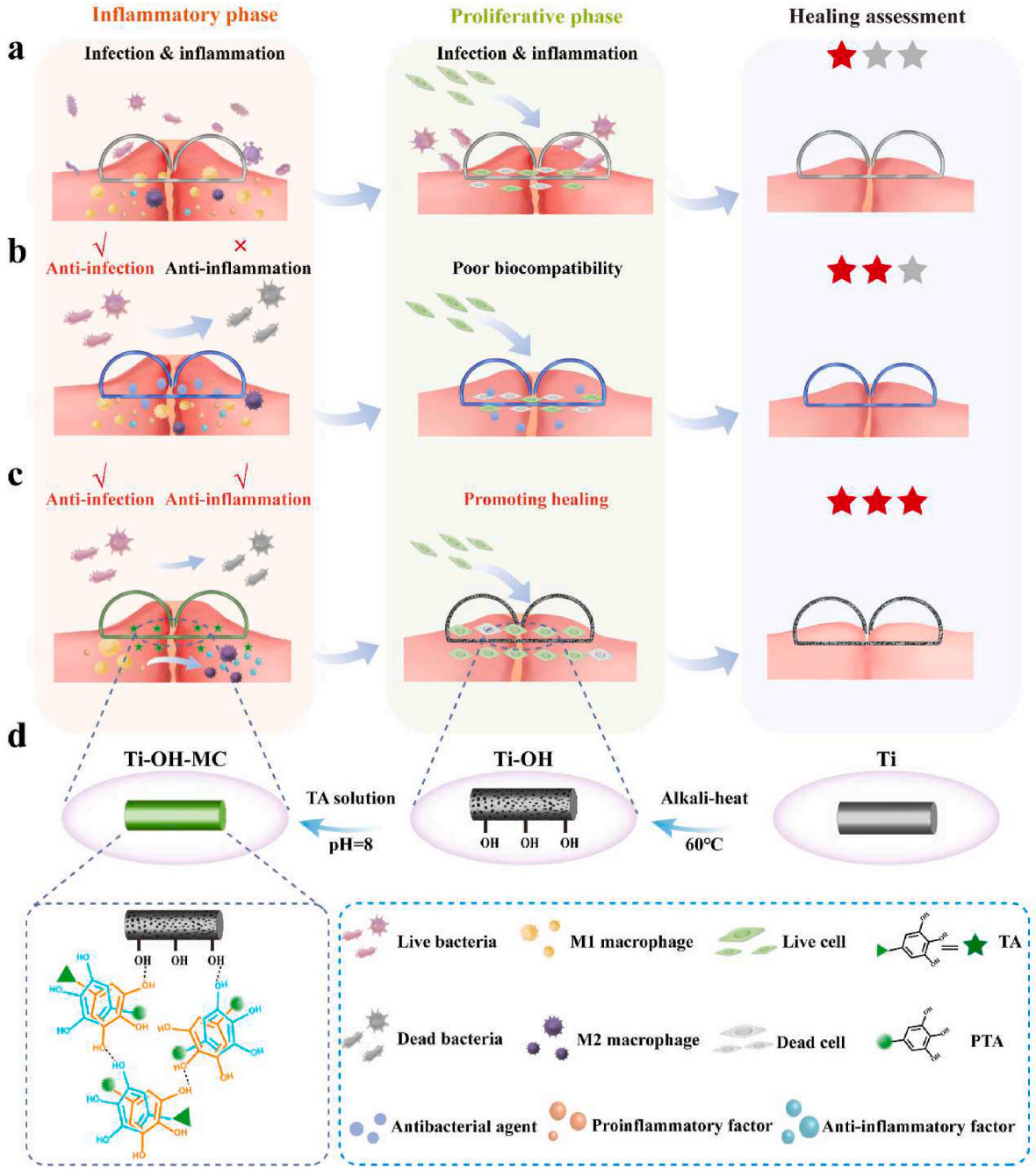

Fig. 1. Schematic illustration of the performance of a) titanium staple, b) antibacterial titanium staple and c) Ti–OH-MC for application to the anastomotic stoma; d) Schematic illustration of the structure and preparation process of Ti–OH-MC.

with multifunctional components to achieve simultaneous antibacterial, anti-inflammatory, and cell proliferation capabilities [22]. However, the previous materials' biological properties lack precise temporal regulation to meet the needs of the tissue repair at different phases. Therefore, the scientific challenge for the implantable titanium anastomotic staple lies in dynamically modulate antibacterial and anti-inflammatory capabilities while promoting cell proliferation, adapted with the progression of the anastomotic stoma healing phases, which means doing the right thing at the right time.

This study aims to illustrate the multifunctional design concept of titanium anastomotic staple through *in vitro* experiment and a rabbit gastrointestinal anastomosis model. The fabrication process involves creating a uniform porous structure on the surface of titanium staple using alkali-heat treatment. Subsequently, a polytannic acid/tannic acid multifunctional coating is applied onto the alkali-heat treated titanium staple with oxidative self-polymerization, hydrogen bonding, and π-π stacking. Importantly, during the early phase of tissue repair, acidic condition caused by infection or inflammation can break hydrogen bonding and π-π stacking between tannic acid molecules and polytannic acid, releasing tannic acid molecules to provide antibacterial and anti-inflammatory, and immune microenvironment regulation functions. Simultaneously, the hydrogen bonding between the multifunctional coating and the titanium staple is also broken to expose the porous structure of the staple, promoting cell adhesion and proliferation during the later proliferation and remodeling phases. This design achieves dynamic sequential regulation between antibacterial, anti-inflammatory, and cell-proliferative properties, facilitating anastomotic stoma repair (Fig. 1c). This fabrication strategy of titanium material is simple and biocompatible, holds promise for industrialization and clinical application. This work addresses the current limitations of conventional anastomotic staple and provides inspiration into the multifunctional design of titanium materials for tissue repair.

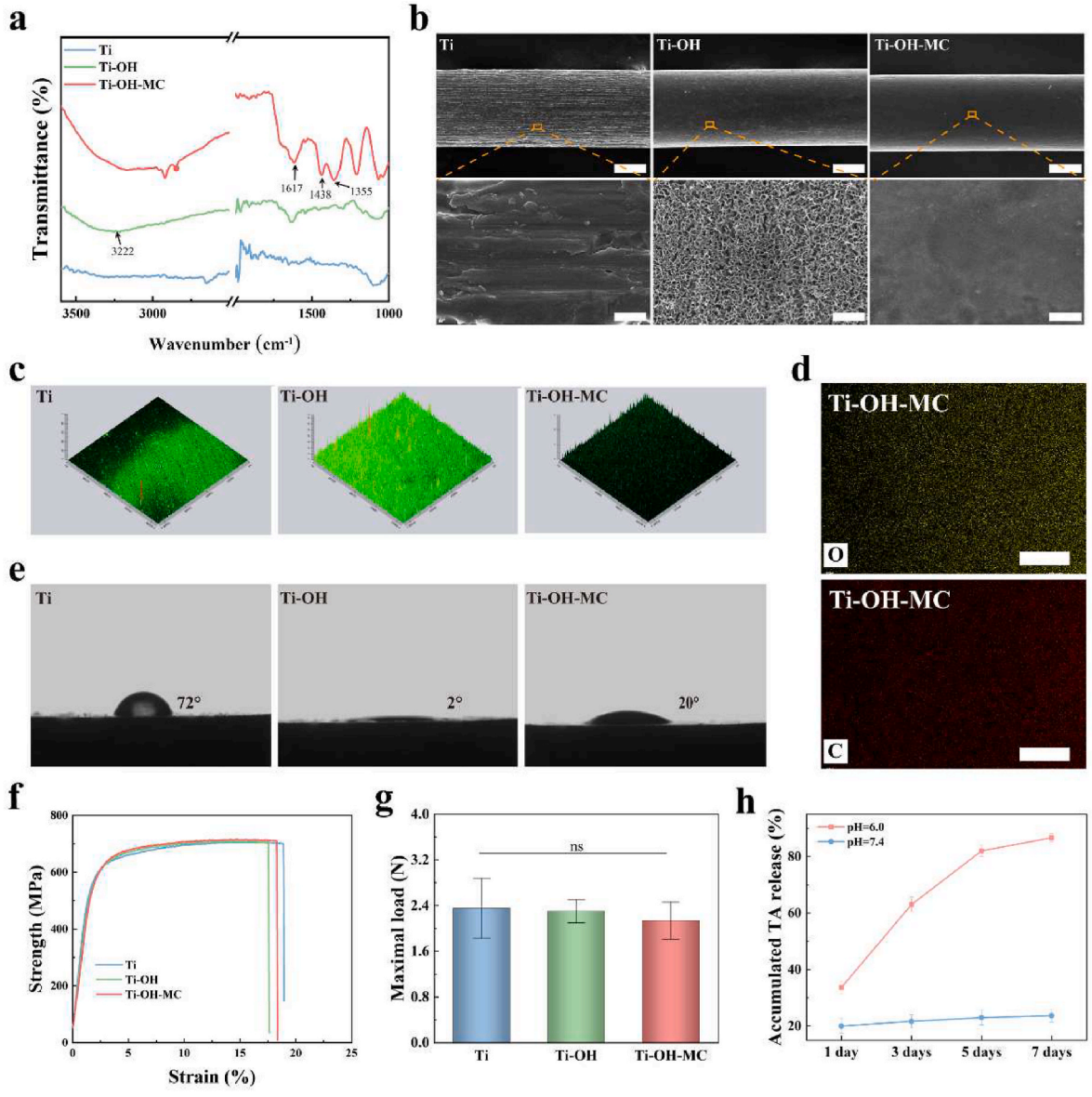

Fig. 2. Structure characterization of Ti–OH-MC. a) FT-IR spectra of Ti, Ti–OH, and Ti–OH-MC; b) SEM images of Ti, Ti–OH, and Ti–OH-MC (upper scale bars = 50 μm, lower scale bars = 1 μm); c) CSLM images of the surface roughness of Ti, Ti–OH, and Ti–OH-MC; d) Elemental mapping images of Ti–OH-MC (scale bars = 50 μm); e) Water contact angles of Ti, Ti–OH, and Ti–OH-MC; f) Tensile test of the Ti, Ti–OH, and Ti–OH-MC; g) Single anastomotic staple tensile strength test of the Ti, Ti–OH, and Ti–OH-MC; h) Accumulated TA release of the Ti–OH-MC in buffer solutions under different pH; $n = 3$; ns = no significance.

2. Results and discussion

2.1. Preparation and characterization of Ti–OH-MC

We constructed multifunctional polymer coating on the surface of titanium staple (Ti) by surface pore-making and tannic acid (TA) oxidative polymerization (Fig. 1d). Surface pore-making *via* alkali-heat treatment provides the Ti with well-developed porosity, high surface area, and –OH to coat more coatings [23]. The polytannic acid (PTA) is then gradually deposited on the surface of alkali-heat treated Ti by oxidative polymerization of TA [24], and the TA is encapsulated in the PTA by hydrogen bonding and π-π stacking simultaneously. The samples obtained by surface pore-making and surface multifunctional coating are referred to as Ti–OH and Ti–OH-MC, respectively. As shown in the FT-IR spectra (Fig. 2a), the peak of Ti–OH at 3222 cm^{-1} reflects the O–H stretching vibration, the peaks at 1617 cm^{-1} and 1438 cm^{-1} in Ti–OH-MC are attributed to the stretching vibration of the benzene skeleton, and the peak at 1355 cm^{-1} belongs to the C–O vibration [25]. The scanning electron microscopy (SEM) images of Ti, Ti–OH, and Ti–OH-MC are displayed in Fig. 2b. Contrary to the smooth, nonporous surface of the Ti, Ti–OH has a porous surface morphology characterized by pore diameters ranging from approximately 65 to 250 nm, resembling a honeycomb-like structure (Fig. 2b and Fig. S1). The Sa value of the Ti-OH (0.77 ± 0.04) is considerably higher than that of Ti (0.25 ± 0.01), while the Sa value of Ti–OH-MC (0.63 ± 0.03) falls between the other two groups (Fig. 2c and Fig. S2). The elemental mapping images (Fig. 2d) show that the elements C and O are uniformly and densely distributed on the surface of the Ti–OH-MC. According to Fig. 2e, the

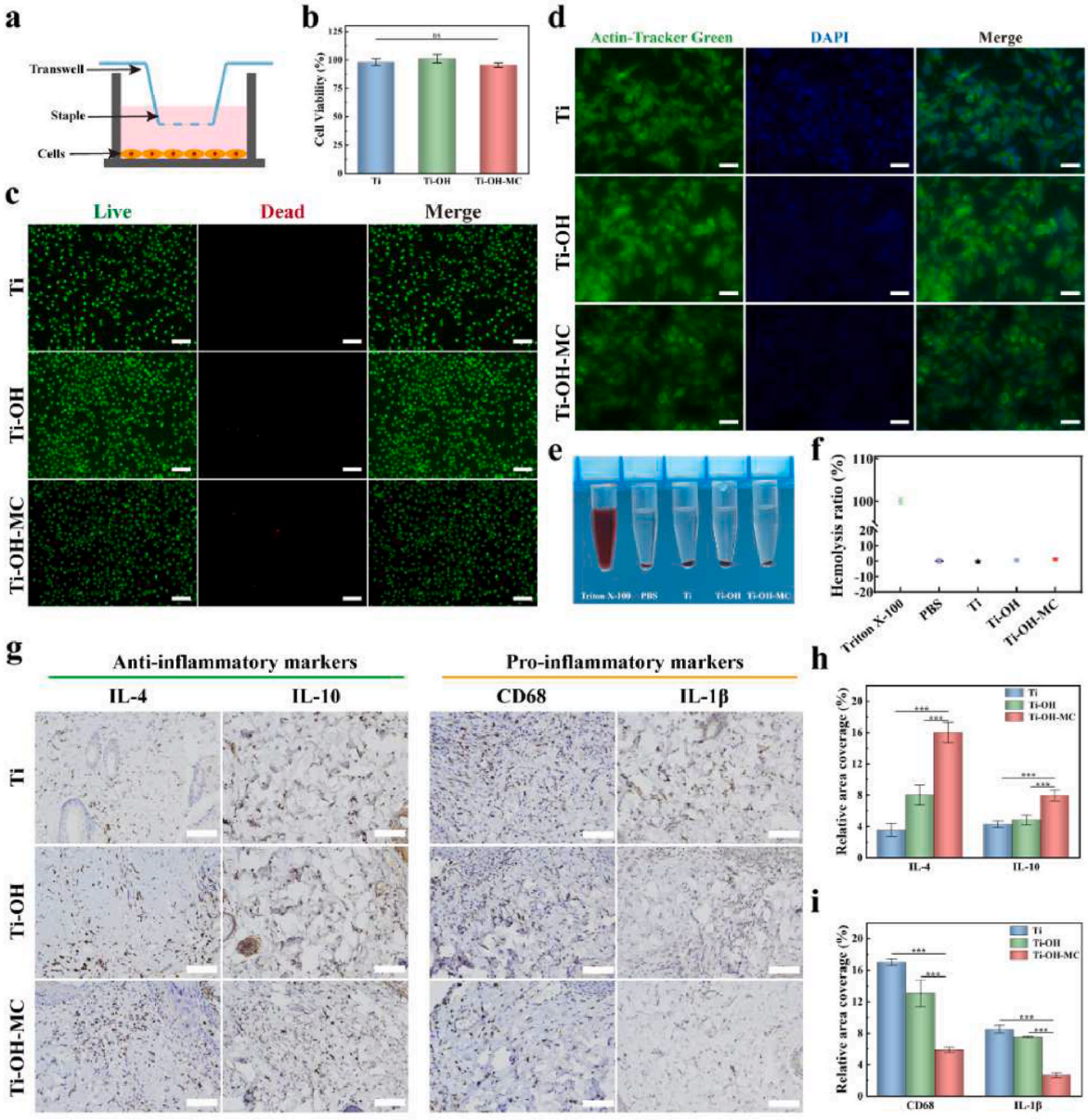

Fig. 3. The biocompatibility of Ti–OH-MC. a) Schematic of the "co-culture with samples" model; b) Cell viability of L929 cells in the Ti, Ti–OH, and Ti–OH-MC groups; c) Live/dead cell staining images of L929 cells in the Ti, Ti–OH, and Ti–OH-MC groups (scale bar: 200 μm); d) Cytoskeleton staining images of L929 cells inm the Ti, Ti–OH, and Ti–OH-MC groups (scale bar: 50 μm); e) Digital phpto of hemolysis tests in the Triton-100, PBS, Ti, Ti–OH, and Ti–OH-MC groups; f) Hemolysis ratios of the Triton-100, PBS, Ti, Ti–OH, and Ti–OH-MC groups; g) Immunohistochemical staining images of IL-4, IL-10, CD68, and IL-1β for Ti, Ti–OH, and Ti–OH-MC after rat subcutaneous implantation for 7 days (scale bar: 100 μm); h) Quantitative analysis of IL-4 and IL-10; i) Quantitative analysis of CD68 and IL-1β; $n = 3$; ns = no significance, $^{***}p < 0.001$.

contact angles of Ti, Ti–OH, and Ti–OH-MC are 72°, 2°, and 20°, respectively. These results confirm that the multifunctional coating is successfully coated on the surface of Ti–OH.

The tensile strength of anastomotic staple is critical to its anastomotic effectiveness [26,27]. The results of the mechanical tensile test show that there is no significant difference in tensile strength between Ti, Ti–OH, and Ti–OH-MC (Fig. 2f). In addition, tensile strength test was performed on a single staple in the anastomosed state to assess the maximum tensile force it could withstand (Fig. S3). The results show that there is also no significant difference among the three anastomotic staples (Fig. 2g). These findings indicate that the pore-making and coating processes do not damage the mechanical properties of the Ti.

During the healing process, anastomotic stoma exhibits varying pH values at different phases. At the inflammatory phase, the pH often assumes a weakly acidic state. However, once the inflammatory phase subsides, the wound environment changes to a neutral state. Therefore, the construction of pH-responsive antibacterial and anti-inflammatory anastomotic staple is of great importance for anastomotic stoma healing. To investigate the pH-responsiveness of the Ti–OH-MC, we simulated an inflammatory environment (pH = 6.0) and a normal physiological environment (pH = 7.4) *in vitro* to evaluate the release behaviors of TA [24,28]. Fig. 2h shows that the percentage of released TA in the inital 2 h approaches 20 % and then remains nearly constant under pH=7.4. In contrast, the Ti–OH-MC releases TA continuously, with complete release occurring by the 7th day under pH=6.0. Apparently, the pH condition exerts a significant influence on the release behaviors of TA. The results confirm the pH-responsiveness of our Ti–OH-MC, which allows for controlled antibacterial and anti-inflammatory properties by regulating the amount of released TA during the inflammatory phase.

2.2. Biocompatibility of Ti–OH-MC

Excellent biocompatibility is an essential property for biomedical materials [29]. To evaluate the biocompatibility of the prepared anastomotic staple, a “co-culture with sample” model was conducted (Fig. 3a) [30]. The CCK-8 kit was used to quantitatively assess the toxicity of the Ti, Ti–OH, and Ti–OH-MC. The results show that the cell viability of all samples exceed 90 % (Fig. 3b). The live/dead cell assay in Fig. 3c shows that most of the L929 cells in the three groups are alive (green fluorescence), with only a few dead cells present (red fluorescence). In addition, the cells in the three groups are densely arranged in a spindle shape, with normal cytoskeletal (green) and nuclear (blue) morphology (Fig. 3d). These results indicate that our Ti–OH and Ti–OH-MC have good cytocompatibility comparable to that of clinical Ti. The hemocompatibility of the Ti–OH-MC was assessed using a hemolysis test. As shown in Fig. 3e, the positive control group (Triton X-100) exhibits a bright red color, indicating significant erythrocyte rupture and hemoglobin release. In contrast, the PBS, Ti, Ti–OH, and Ti–OH-MC groups show no color change, with hemolysis percentages of less than 5 %, indicating excellent hemocompatibility (Fig. 3f). Furthermore, the inflammatory response of the prepared anastomotic staple was evaluated by a rat subcutaneous implantation model. The results of immunohistochemistry indicate that (Fig. 3g), in comparison to the Ti and Ti–OH groups, the expression of the pro-inflammatory markers (CD68 and IL-1β) in the Ti–OH-MC group is significantly decreased (Fig. 3i), while that of anti-inflammatory markers (IL-4 and IL-10) is significantly increased (Fig. 3h). The above results confirm the ideal biocompatibility of our Ti–OH-MC.

2.3. Antibacterial property of Ti–OH-MC

Bacterial metabolism can induce a weakly acidic microenvironment, which has a pH value of 5.0–6.5. In such microenvironment, the hydrogen bonding between TA and PTA is disrupted, leading to the release of TA [24]. TA has been found to interrupt the bacterial biological activity by different mechanisms including iron chelation, inhibition of cell wall synthesis, and disruption of the cell membrane [31,32]. We compared the antibacterial effects of Ti–OH-MC against three type of common bacteria causing anastomotic infections (*S. aureus*, *E. coli*, and *E.faecalis*) with the Ti and Ti–OH. After 12 h of co-culturing, the culture medium in the Ti–OH-MC group exhibits transparency, signifying minimal bacterial growth, whereas the medium in the Ti and Ti–OH groups appear turbid, indicating significant bacterial growth (Fig. 4a). Fig. 4b shows that Ti–OH-MC exhibits almost 100 % killing efficiency against the three bacteria, outperforming the Ti and Ti–OH groups. The results of the long-lasting antibacterial test demonstrate that Ti–OH-MC group still has a good antibacterial ratios on the 5th day (*S. aureus*, 78.3 %; *E. coli*, 69.7 %; *E.faecalis*, 71.3 %) (Fig. 4c). Therefore, our Ti–OH-MC has long-lasting and broad-spectrum antibacterial properties.

2.4. Antioxidant and anti-inflammatory properties of Ti–OH-MC

Excessive inflammation at the anastomotic stoma can significantly hinder anastomotic healing [33]. In addition, inflammation always produces an overabundance of reactive oxygen species (ROS), which directly degrade nucleic acids, proteins, and lipids, causing irreversible damage to the organism [30,34]. TA-based coatings are promising for the treatment of inflammation, as TA is a natural anti-oxidant [35]. The free radical scavenging capacities of Ti–OH-MC against 2,2-diphenyl-1--picrylhydrazyl (DPPH) and 2,2'-azino-bis (3-ethylbenzothiazoline-6-sulfonic acid) (ABTS) were evaluated in this study. As shown in Fig. 4d and e, Ti–OH-MC exhibits enhanced scavenging capabilities for DPPH and ABTS compared to Ti and Ti–OH, indicating improved antioxidant activity. The cellular antioxidant performance of Ti–OH-MC was also evaluated by co-culturing it with L929 cells or Raw264.7 cells exposed to 100 μM H_2O_2, with Ti, Ti–OH as control groups. As shown in Fig. 4f and g, significantly higher cell survival ratios are observed in the L929 cells and RAW 264.7 cells groups treated with the Ti–OH-MC compared to the Ti and Ti–OH groups, indicating that the Ti–OH-MC can scavenges the free radicals produced by H_2O_2. We further used 2′,7′-dichlorodihydrofluorescein diacetate (DCFH-DA) fluorescent probe and flow cytometry to measure the intracellular ROS levels. The fluorescence microscopic images (Fig. 4h and i) show that the Ti and Ti–OH groups exhibit more intense green fluorescence, whereas the Ti–OH-MC group exhibits decreased green fluorescence. The flow cytometry tests also show that the fluorescence intensities of RAW 264.7 and L929 cells in the Ti and Ti–OH groups are higher than those in the Ti–OH-MC group (Fig. S4), indicating that Ti–OH-MC can significantly reduce the intracellular ROS levels. These results demonstrate the excellent antioxidant capacity of Ti–OH-MC.

2.5. In vitro macrophage phenotype regulation of Ti–OH-MC

As vital components of the innate immune system, macrophages play a crucial role in protecting the host, modulating the immune response, and promoting wound healing [36]. *In vitro* co-culture experiments were performed to investigate the potential of Ti– OH-MC to induce macrophage polarization from the M1 to the M2 phenotype. As shown in Fig. 5a, the immunofluorescence staining images indicate significantly higher expression of CD206, a marker of M2 macrophages, in the Ti–OH-MC group compared to the Ti and Ti–OH groups (Fig. S5). We then evaluated the effect of Ti–OH-MC on various inflammatory factors using ELISA test kits. As shown in Fig. 5b, LPS treatment results in excessive production of pro-inflammatory cytokines, with the expression levels of TNF-α and IL-6 (secreted by M1 macrophages) being 4.90 ± 0.46 ng mL^{-1} and 11.40 ± 1.25 ng mL^{-1}, respectively. Both Ti and Ti–OH have no significant down-regulating effect on pro-inflammatory cytokines. In contrast, Ti–OH-MC can down-regulate the expression levels of TNF-α and IL-6 to 0.77 ± 0.06 ng mL^{-1} and 2.17 ± 0.12 ng mL^{-1}, respectively. Meanwhile, the expressions of anti-inflammatory

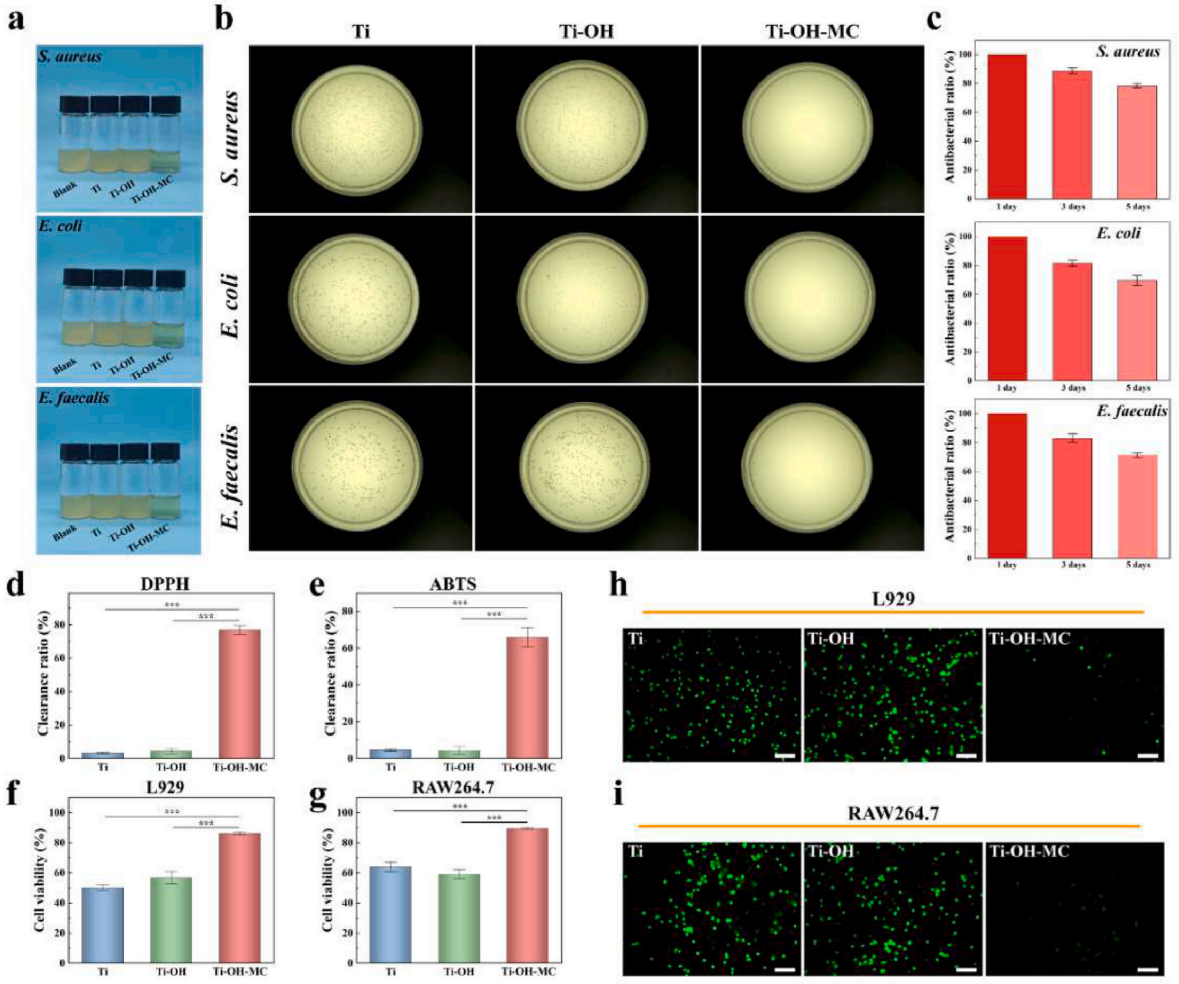

Fig. 4. *In vitro* antibacterial and antioxidant properties. a) Digital photos of *S. aureus*, *E. coli*, and *E.faecalis* suspensions cocultured with the Ti, Ti–OH, and Ti–OH-MC after 12 h; b) Digital photos of the viable bacterial clones formed by *S. aureus*, *E. coli*, and *E.faecalis* on agar plates after 12 h contact with Ti, Ti–OH, and Ti–OH-MC; c) The antibacterial ratios of the Ti–OH-MC for *S. aureus*, *E. coli*, and *E.faecalis* after 1, 3, and 5 days of incubation; d-e) The results of Ti, Ti–OH, and Ti–OH-MC on scavenging DPPH (d) and ABTS (e) radicals; f-g) Cell viability of L929 cells (f) and RAW 264.7 cells (g) co-cultured with Ti, Ti–OH, and Ti–OH-MC for 12 h in a medium containing H_2O_2; h-i) Fluorescence images illustrating intracellular ROS reduction in H_2O_2-stimulated L929 cells (h) and RAW 264.7 cells (i) (scale bar: 200 μ m) when co-cultured with Ti, Ti–OH, and Ti–OH-MC; $n = 3$; $^{***}p < 0.001$.

cytokines were examined. In the LPS group, the expression levels of IL-10 and IL-4 (secreted by M2 macrophages) are 30.37 ± 1.70 ng mL^{-1} and 20.40 ± 2.05 ng mL^{-1}, respectively. The expression levels in the Ti and Ti–OH groups are similar to those in the LPS group. In contrast, the expression levels of IL-10 and IL-4 increased to 54.03 ± 3.09 ng mL^{-1} and 47.63 ± 1.27 ng mL^{-1} in the Ti–OH-MC group (Fig. 5c). These results clearly indicate that Ti–OH-MC can effectively promote macrophage polarization from the M1 to the M2 phenotype, thereby down-regulating pro-inflammatory cytokines and up-regulating anti--inflammatory cytokines.

RNA sequencing was used to evaluate the messenger RNA (mRNA) levels of M1 macrophages after co-culture with Ti–OH-MC for 24 h. The transcriptomic profiles of M1 macrophages and Ti–OH-MC-treated M1 macrophages were compared with differential expression assessment, Gene Ontology (GO) enrichment studies, and Kyoto Encyclopedia of Genes and Genomes (KEGG) pathway-based analyses. The Venn diagram (Fig. 5d) shows that 18381 genes are shared between the M1 and Ti–OH-MC groups, with the M1 group having 2794 exclusive genes and the Ti–OH-MC group having 1834 unique genes. The volcano plot (Fig. 5e) shows the distribution of differentially expressed genes (DEGs) between the M1 and Ti–OH-MC groups. A total of 692 DEGs were detected in Ti–OH-MC group, with 497 genes up-regulated and 195 genes down-regulated. The GO enrichment analysis of these DEGs includes biological process, cellular components, and molecular functions (Fig. 5f–h). The biological process analysis reveals that Ti–OH-MC may regulate macrophage polarization through the regulation of JNK cascade. The cellular component (CC) analysis shows that the DEGs are associated with the inflammasome complex, suggesting that Ti–OH-MC may modulate the expression of inflammatory factors *via* regulation of the inflammasome complex. Molecular function (MF) results show that differential gene expression is associated with immune receptor activity, further demonstrating that Ti–OH-MC can regulate immune function by affecting immune receptor activity. Studies have shown that the Notch signaling pathway is one of the major pathways regulating macrophage polarization, which not only influences the differentiation of immune cells, but also regulates the functional states [37]. The KEGG pathway enrichment analysis in Fig. 5i shows that the DEGs are associated with the Notch signaling pathway. The above results indicate that our Ti–OH-MC probably accelerates the healing of the anastomotic stoma by activating the Notch signaling pathway to promote the polarization of macrophages from the M1 phenotype to the M2 phenotype and alleviate inflammation.

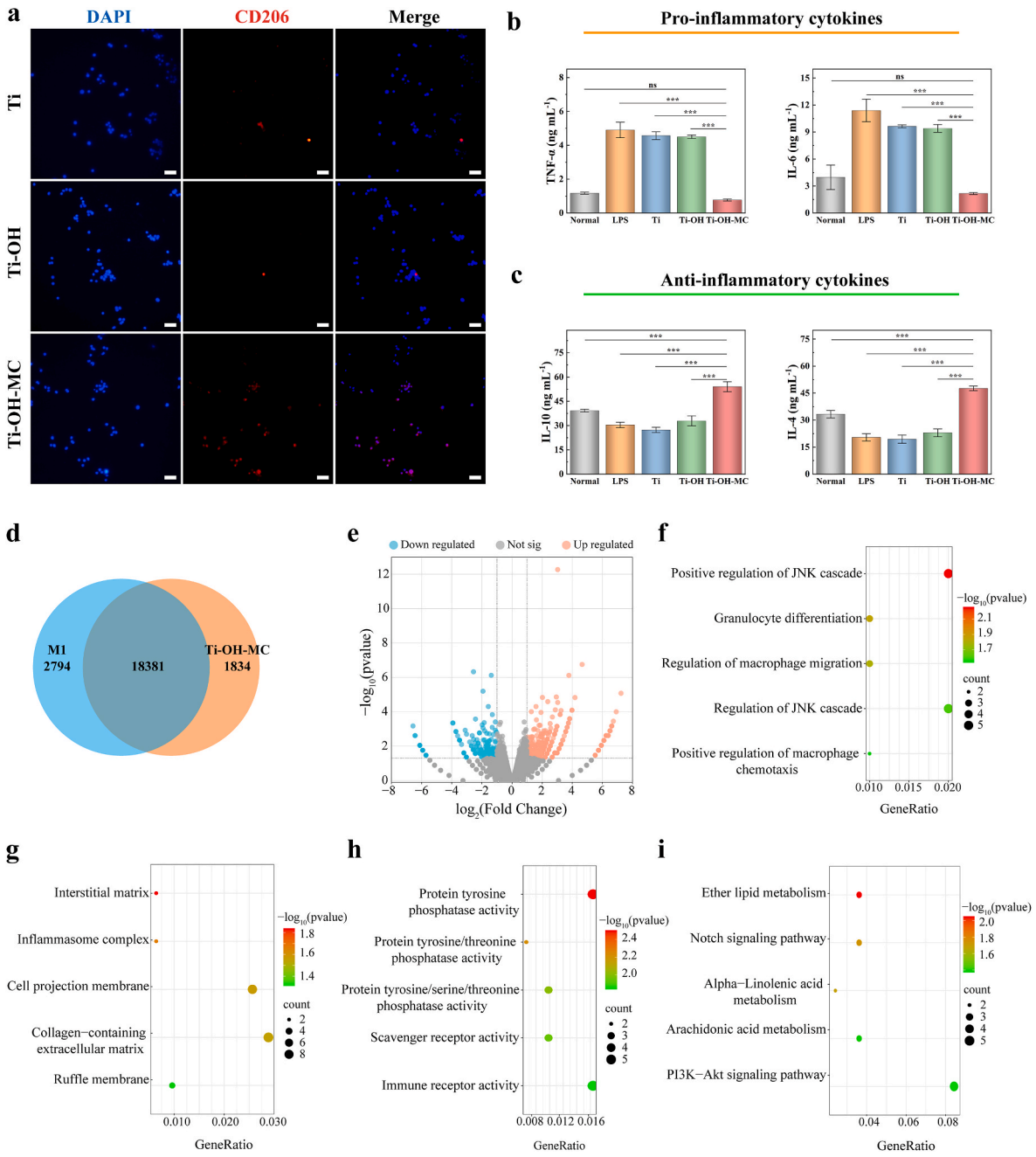

Fig. 5. Pro-macrophage polarization properties *in vitro*. a) Immunofluorescence staining (DAPI and CD206) images of M1 macrophages after co-culture with Ti, Ti–OH, and Ti–OH-MC (scale bars: 100 μm); b) Expression levels of TNF-α and IL-6 in Normal, LPS, Ti, Ti–OH, and Ti–OH-MC groups; c) Expression levels of IL-10 and IL-4 in Normal, LPS, Ti, Ti–OH, and Ti–OH-MC groups; d) Venn diagram of differential gene counts in the M1 and Ti–OH-MC groups; e) Volcano plot of differentially expressed genes; f-h) GO enrichment analysis of the DEGs (f: Biological Process, g: Cell Component, h: Molecular Function); i) KEGG pathway analysis of the DEGs; $n = 3$; ns = no significance, $*p < 0.05$, $**p < 0.01$, $***p < 0.001$.

2.6. Enhancement of cell adhesion and proliferation properties of Ti–OH-MC

The adhesion and proliferation capacities of cells are critical for anastomotic stoma healing. In order to evaluate the effects of Ti–OH-MC on cell adhesion and proliferation, we co-cultured the Ti–OH-MC after soaking in PBS (pH = 6) for different times with cells. As shown in Fig. 6a, after 3 days of immersion, the coating of Ti–OH-MC disintegrated, and the porous surface was exposed partially. By day 7, the multifunctional coating completely delaminates, and the entire porous surface was exposed. The Ti–OH-MC after immersion in PBS for 3 days and 7 days are named as Ti–OH-MC-3d and Ti–OH-MC-7d, respectively. When Ti, Ti–OH, Ti–OH-MC-3d, and Ti–OH-MC-7d are co-cultured with L929 cells, it is found that more cells adhere to samples with more pores, indicating that the porous structure formed by alkali treatment effectively promotes the cell adhesion and proliferation (Fig. 6b). The semi-quantitative analysis results reveal that the fluorescence area of the Ti–OH-MC-7d group (59.60 ± 4.09 %) is higher than that of the Ti (3.27 ± 0.45 %) and Ti–OH-MC-3d (13.28 ± 2.20 %) groups (Fig. S6). Nanoscale porous surface has been demonstrated to effectively regulate cellular behavior, potentially by altering the spatiotemporal dynamics within cells and influencing the sensing behavior of intracellular mechanosensors [38,39]. Furthermore, compared to smooth substrates, nanoscale porous surface exhibits a pronounced upregulation of integrin

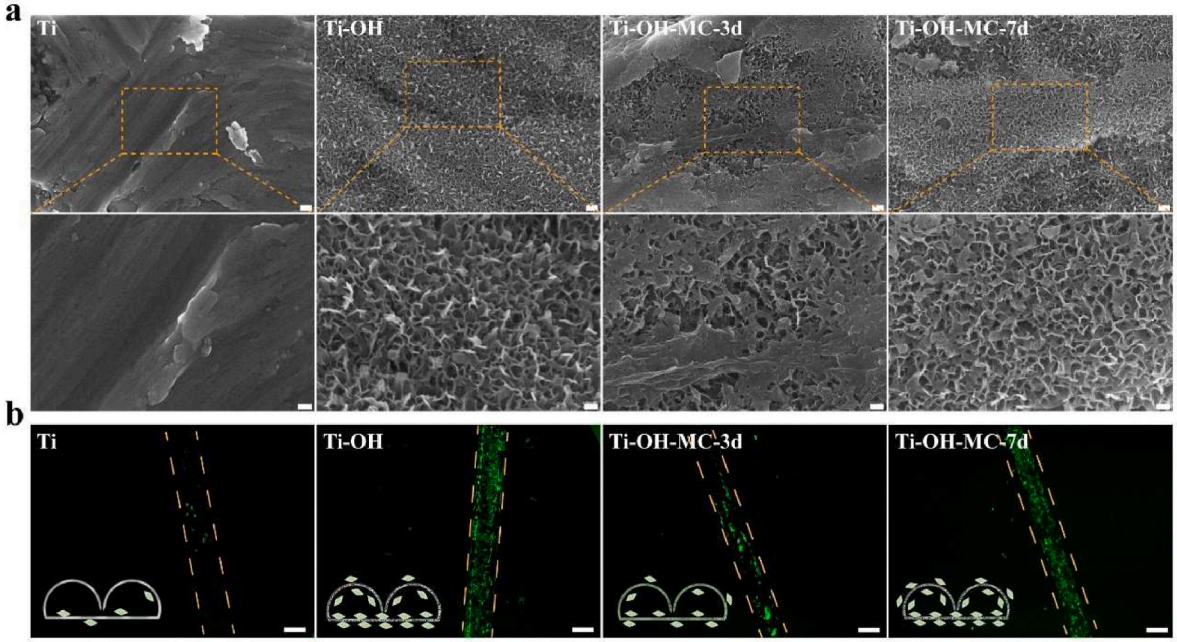

Fig. 6. A) SEM images of Ti, Ti–OH, Ti–OH-MC-3d, and Ti–OH-MC-7d (upper scale bar: 500 nm; lower scale bar: 200 nm); b) Fluorescent images of cell adhesion (scale bar: 200 μm) of Ti, Ti–OH, Ti–OH-MC-3d, and Ti–OH-MC-7d.

expression, thereby enhancing cell adhesion, which is critical for tissue repair [40,41]. The delamination of the coating on Ti–OH-MC coincides well with the healing phase of the anastomotic stoma, which can also effectively promote anastomotic stoma healing during the proliferative phase.

2.7. *In vivo animal surgery*

The promising *in vitro* results have motivated us to further investigate the therapeutic efficacy of Ti–OH-MC in a more complex *in vivo* environment. A rabbit model of gastrointestinal anastomosis was established as shown in Fig. 7a and Fig. S8. Tissue samples from the anastomotic stoma were collected on days 3, 7, and 14 to monitor the progress of anastomotic stoma healing and assess the effect of Ti–OH-MC on the three phases of tissue repair (inflammatory phase, proliferative phase, and remodeling phase, as depicted in Fig. 7b). The initial inflammatory phase of anastomotic stoma healing, which typically lasts 3–5 days, is characterized by inflammatory cells infiltration and elevated levels of pro-inflammatory cytokines. Immunohistochemical staining was conducted to evaluate inflammatory state by assessing the expression of pro-inflammatory cytokines interleukin-6 (IL-6) and tumor necrosis factor alpha (TNF-α), as well as anti-inflammatory cytokines transforming growth factor-β (TGF-β) and interleukin-10 (IL-10) (Fig. 7c). In comparison to the Ti and Ti–OH groups, the expression levels of IL-6 and TNF-α are significantly decreased in the Ti–OH-MC group (Fig. 7f and g). Conversely, the expression levels of TGF-β and IL-10 are significantly increased in the Ti–OH-MC group (Fig. 7h and i). These results indicate that Ti–OH-MC shows desirable anti-inflammatory properties during the inflammatory phase to accelerate the transition of the anastomotic stoma from the inflammatory phase to the proliferative phase. During the proliferative phase, neovascularization plays a critical role in ensuring the transport of nutrients and oxygen to the anastomotic stoma, supporting fibroblast proliferation and collagen synthesis. The results of platelet endothelial cell adhesion molecule 1 (CD31) immunostaining indicate that the amount of neovascularization in the Ti–OH-MC group is significantly higher than that in the Ti and Ti–OH groups (Fig. 7j). In the remodeling phase, proper collagen deposition and remodeling are crucial for improving tissue strength and healing. The results of Masson staining reveal higher levels of collagen expression in the Ti–OH-MC group compared to the Ti and Ti–OH groups (Fig. 7k). These results provide evidence that Ti–OH-MC exerts various beneficial effects, including reducing inflammation, promoting neovascularization, and accelerating collagen deposition, thereby offers a promising approach to improve anastomotic stoma healing.

The burst pressure test is a crucial method for evaluating the healing degree of anastomotic stoma [26]. As shown in Fig. 7l, the ability of an anastomotic stoma to withstand burst pressure increases as it gradually heals. Specifically, the burst pressure of the Ti–OH-MC group on day 7 is 26.4 ± 0.6 kPa, and further increases to 36.1 ± 0.8 kPa on day 14. In comparison, the burst pressure of the Ti group is 17.7 ± 0.6 kPa on day 7 and 27.7 ± 0.9 kPa on day 14. Similarly, the burst pressure of the Ti–OH group is 20.8 ± 0.5 kPa on day 7 and 28.3 ± 0.3 kPa on day 14. The results confirm that the Ti–OH-MC group exhibits superior healing of the anastomotic stoma, and the comparison of bursting pressure is statistically significant.

Peripheral blood was collected from the rabbits on preoperative day 1 (Pre-1) and postoperative days 3, 7, and 14 for the detection of physiological indicators. The results indicate that the white blood cell count (normal value:3–13.5*10^9 L^{-1}) in the Ti–OH-MC group is lower than that in the Ti and Ti–OH groups on days 3, 7, and 14 (Fig. 7m), suggesting that Ti–OH-MC has an ideal regulatory effect on inflammation. Activated partial thromboplastin time (APTT), thrombin time (TT), and fibrinogen (FBg) were used to assess coagulation function of the rabbits, while alanine aminotransferase (ALT) and aspartate aminotransferase (AST) were used to evaluate liver function. There are no significant differences in coagulation and liver function among the Ti, Ti–OH, and Ti–OH-MC groups (Figs. S9 and 10). These findings further suggest the excellent biocompatibility of Ti–OH-MC, indicating that the presence of the multifunctional coating does not induce coagulation and liver dysfunction.

3. Conclusion

In conclusion, a novel anastomotic staple, combining a multifunctional coating with a porous surface structure, has been successfully fabricated in our study. This innovative design enables the anastomotic

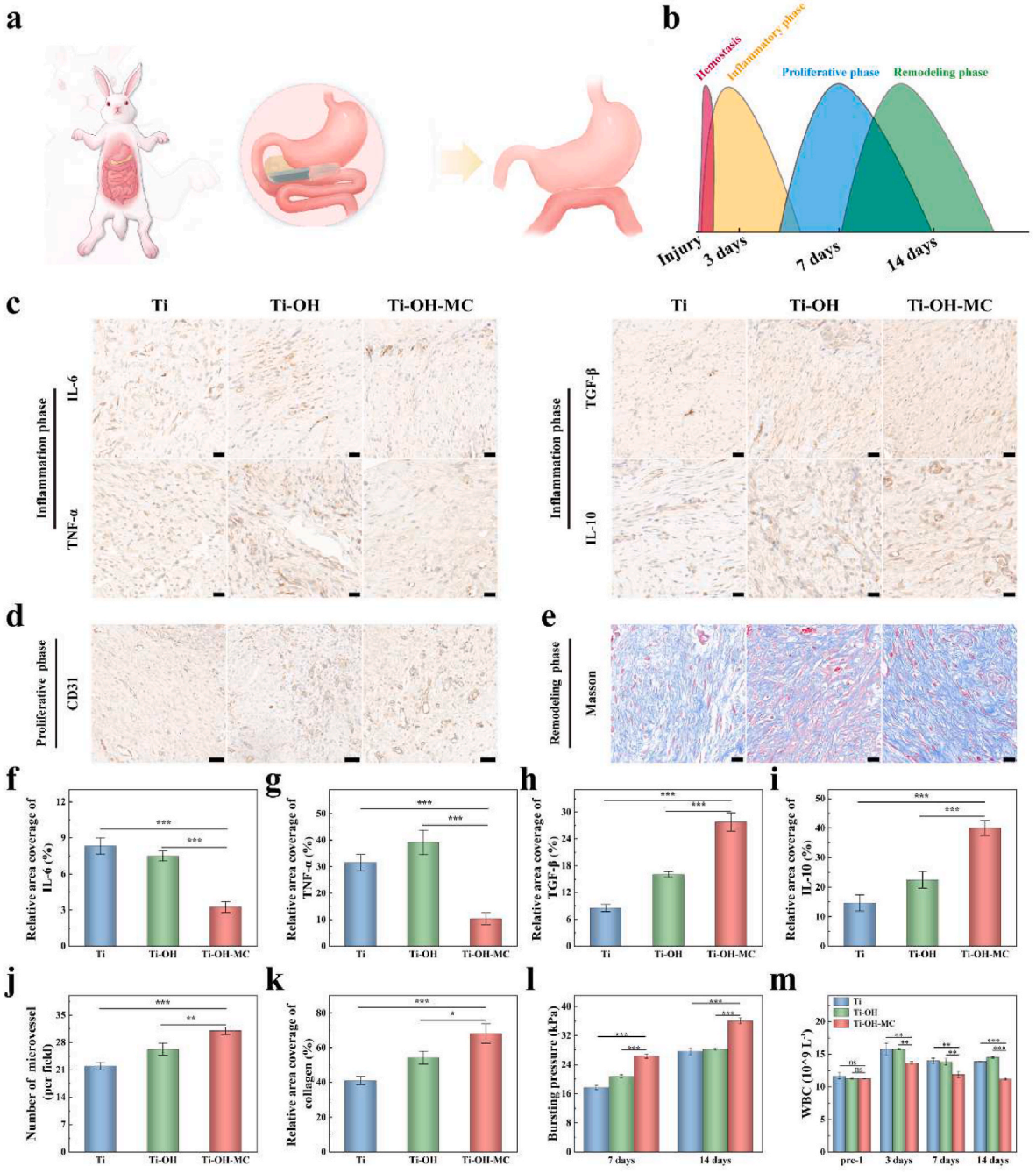

Fig. 7. A) Schematic diagram of gastrointestinal anastomosis in rabbit; b) Schematic of anastomotic stoma healing progress; c) Immumohistochemical staining images of IL-6, TNF-α, TGF-β, and IL-10 at the anastomotic stoma on day 3 (scale bar: 20 μm); d) Immumohistochemical staining images of CD31 on day 7 at the anastomotic stoma (scale bar: 50 μm); e) Masson staining images on day 14 at the anastomotic stoma (scale bar: 20 μm); f) Statistical analysis of IL-6 expression; g) Statistical analysis of TNF-α expression; h) Statistical analysis of TGF-β expression; i) Statistical analysis of IL-10 expression; j) Statistical analysis for the number of blood vessel; k) Statistical analysis of collagen expression; l) Statistical analysis of bursting pressure on days 7, and 14; m) Statistical analysis of WBC on days pre-1, 3, 7, and 14; $n = 3$, $^{*}p < 0.05$, $^{**}p < 0.01$, $^{***}p < 0.001$.

staple to intelligently respond to the microenvironment of the anastomotic stoma, dynamically adapt to the healing phases of the anastomotic stoma, and comprehensively meet its “step by step” requirements for antibacterial, anti-inflammatory, and cell proliferation effects. During the inflammatory phase, the multifunctional coating gradually disintegrates under the influence of a weak acidic environment, and the released TA has potent antibacterial and anti-inflammatory properties, promoting the polarization of macrophages towards the M2 phenotype and reversing the "pro-inflammatory" state, which is detrimental to anastomotic healing. Meanwhile, disintegration of the coating exposes the porous surface structure of Ti-OH-MC, which can enhance cell adhesion and tissue regeneration, further promoting anastomotic healing during the proliferative phase. Therefore, the dynamic transition of its biological activity provides a potential strategy to address the early phase requirements for resistance to infection and inflammation, as well as the later phase requirements to promote healing. The *in vivo* gastrointestinal anastomosis experiment in New Zealand rabbits shows that Ti–OH-MC significantly promotes the anastomotic stoma healing. This study provides an effective strategy for the precise coupling and sequential combination of contradictory biological activities and has

important implications for the design of anastomotic staples for gastrointestinal anastomosis.

4. Materials and method

4.1. Materials

Tannic acid (TA) was purchased from Shanghai Macklin Biochemical Technology Co., Ltd. (China). Ti staples, disposable endoscope linear cutting staplers, and components (Fig. S7) were provided by Jiangsu Channel Medical Device Co., Ltd. (China). Ti desks were purchased from Guangzhou Lige Technology Co., Ltd. (China). *Staphylococcus aureus* (*S. aureus*, ATCC 25923) and *Escherichia coli* (*E. coli*, ATCC 25922) were obtained from the department of laboratory medicine, Guangdong Provincial People's Hospital (China). *Enterococcus faecalis* (*E. faecalis*, BNCC337174) was purchased from Beina Biotechnology Co., Ltd. (China). Dulbecco's modified Eagle's medium (DMEM), fetal bovine serum (FBS), and penicillin-streptomycin solution were provided by Gibco BRL (USA). Cell counting kit-8 (CCK-8) was purchased from Labgic Technology Co., Ltd. (China). Live/dead cell viability kit (Calcein-AM/PI) was purchased from Shanghai Xinyu Biotechnology Co., Ltd. (China). Actin-Tracker Green-488 was purchased from Beyotime Biotech Inc. (China). Standard fibroblast cell line L929 fibroblasts and mouse macrophages (Raw264.7) were purchased from Jiangsu Keygen Biotech Co., Ltd. (China). Rabbit blood was purchased from Guangzhou Hongquan Biotechnology Co., Ltd. (China). Rabbit polyclonal antibody to CD206 and Cy3-labeled goat anti-rabbit IgG were purchased from Wuhan Servicebio Technology Co., Ltd. (China). All solvents and chemicals were purchased from commercial sources and used as received, unless otherwise noted. The Sprague Dawley (SD) rats and New Zealand rabbits were purchased from Huateng BioScience Co., Ltd. (China). All rats and rabbits were fed and tested in accordance with laboratory rules and guidelines. Gene sequencing and histological analysis were conducted by Wuhan Servicebio Technology Co., Ltd. (China).

4.2. Sample preparation

The titanium (Ti) substrates were polished in steps using various SiC sandpapers ranging from 400# to 1500#, ultrasonically cleaned for 15 min with acetone, ethanol, and distilled respectively, and then air dried. Afterwards, the Ti samples were alkaline heat treated using 5 M NaOH at 60 °C with agitation at 100 rpm for 24 h, and washed by distilled water and vacuum drying to obtain the alkali-heated Ti samples (Ti–OH). Subsequently, the Ti–OH samples were immersed in TA solution (60 mg mL^{-1}) at pH 8.0 for 2 h to obtain the Ti–OH-MC samples. The Ti samples for the experiment were as follows: titanium wire with a diameter of 0.1 mm for tensile test; titanium disks with 2 mm in height, 10 mm in diameter for Fourier transform infrared (FT-IR), Atomic Force Microscope (AFM) and *in vivo* subcutaneous implantation experiment; Ti anastomotic staples for other experiments.

4.3. Structure characterizations

FT-IR spectra were recorded using an FT-IR spectrometer (Nicolet IS50, Thermo Scientific, USA). Surface morphologies and elemental mapping images were examined by field-emission scanning electron microscopy (FESEM, Sigma 300, Zeiss, Germany). Roughness measurements were performed with a confocal laser scanning microscope (CLSM; LSM 700, Zeiss, Germany) and the Sa (Arithmetical Mean Height) parameter was obtained by AFM (Asylum Research MFP-3D, Oxford Instrument, UK). Water contact angles were measured using a drop shape analyzer (DSA 100, Kruss, Germany). Mechanical tests were conducted on an electronic universal test machine (WD-5A, Guangzhou Guangshi Instrument Co., Ltd., Guangzhou, China).

4.4. In vitro release of TA

Ti–OH-MC was immersed in 2 mL of phosphate-buffered Saline (PBS) solution (pH:6.0 and 7.4) at 37 °C. On days 1, 3, 5, and 7, 2 mL of supernatant was collected for TA content measurement while an equal volume of fresh buffer solution was added to the solutions. The supernatant was analyzed by UV–Vis spectrometer to determine the TA content.

4.5. Biocompatibility of Ti–OH-MC

The cell counting kit-8 reagent (CCK-8) was conducted to evaluate the cell cytotoxicity and proliferation. L929 cells were co-cultured with the sterilized Ti, Ti–OH, and Ti–OH-MC samples and incubated at 37 °C for 24 h. CCK-8 (10 %) solution was then added and kept in the dark for 1 h. The absorbance of the resulting solution at 450 nm was measured using a full wavelength microplate reader (Multiskan Go, Thermo Scientific, USA). Live/dead staining kits were performed for L929 cell staining. Briefly, L929 cells were co-cultured with Ti, Ti–OH, and Ti–OH-MC samples and incubated at 37 °C for 24 h. After incubation, live and dead cells were stained using a Calcein-AM/PI staining kit according to the manufacturer's instructions. Images were captured with a fluorescence microscope (ZEISS Axio Observer Z1, Germany). The protocol of cytoskeleton staining is as follows: L929 cells were co-cultured with Ti, Ti–OH, and Ti–OH-MC samples and incubated at 37 °C for 24 h. The cells were then fixed with 4 % paraformaldehyde for 10 min, followed by 3 washes with PBS (each lasting for 3 min). Permeabilization was achieved with 0.1 % Triton X-100 for 5 min, followed by a further 3 washes with PBS. The cells were then sequentially stained with Actin-Tracker Green working solution (200 μL) and counterstained with DAPI (200 μL), each followed by 3 washes with PBS. Finally, fluorescence images were captured using a fluorescence microscope (ZEISS Axio Observer Z1, Germany).

The hemolytic activity assay was conducted to assess the hemocompatibility of Ti, Ti–OH, and Ti–OH-MC. Briefly, rabbit blood was centrifuged at 1500 rpm for 5 min to obtain erythrocytes. The erythrocytes were washed 3 times and diluted to a concentration of 5 % (v/v) with PBS. The Ti, Ti–OH, and Ti–OH-MC samples were then co-cultured with 500 μL erythrocyte suspension (5 % v/v) in tubes for 1 h at 37 °C. The supernatant was then collected to measure absorbance at 540 nm using a microplate reader (Multiskan Go, Thermo Scientific, USA). 0.1 % Triton X-100 was used as a positive control and PBS was used as a negative control. The hemolysis ratio (HR) was calculated according to Eq. (1):

$$HR = \frac{OD\ of\ Sample - OD\ of\ negative\ control}{OD\ of\ positive\ control - OD\ of\ negative\ control} \times 100\% \quad (1)$$

Histocompatibility test was performed by implanting samples subcutaneously into the dorsal side of the rat. On day 7 after implantation, the dorsal tissues were collected, fixed, dehydrated, and subjected to immunohistochemical staining. The expression levels of the pro-inflammatory markers (CD68 and IL-1β) and the anti-inflammatory markers (IL-4 and IL-10) were analyzed.

4.6. Antibacterial property of Ti–OH-MC

To assess the antibacterial properties, the plate count method was performed to quantify the number of colony forming units (CFU) on agar plates. *S. aureus*, *E. coli*, and *E.faecalis* were cultured in Luria-Bertani (LB) growth medium overnight at 37 °C in a shaking incubator. Subsequently, the sterilized Ti, Ti–OH, and Ti–OH-MC samples were placed in a 24-well plate and immersed in 300 μL of *S. aureus*, *E. coli*, and *E.faecalis* (10^6 CFU mL^{-1}) respectively, followed by incubation at 37 °C for 12 h. The supernatants from each sample were then diluted 10^6-fold with PBS, and subsequently inoculated onto agar plates using a volume of 20 μL from the diluted bacterial suspension. After a further incubation of 12 h,

the bacterial CFU were photographed. The antibacterial ratio (AR) was calculated using Eq. (2):

$$AR = \frac{CFU\ of\ blank - CFU\ of\ sample}{CFU\ of\ blank} \times 100\% \quad (2)$$

The turbidity of the bacterial solutions was observed. The Ti, Ti–OH, and Ti–OH-MC samples were sterilized by UV irradiation for 1 h and added to small glass bottles containing *S. aureus*, *E. coli*, and *E.faecalis* suspensions (10^8 CFU mL^{-1}) respectively. The small glass bottles were then incubated at 37 °C for 12 h. In this assay, an untreated bacterial solution was used as a blank group. Photographs were taken to record the turbidity of the bacterial suspensions.

For the long-lasting antibacterial test, the sterilized Ti–OH-MC samples were placed in a 24-well plate, immersed in 300 μL of *S. aureus*, *E. coli*, and *E.faecalis* suspensions (10^6 CFU mL^{-1}) respectively and then added to a fresh bacterial solution every 24 h for 5 days. The antibacterial ratios on days 1, 3, and 5 were calculated using the plate count method described above.

4.7. Antioxidant and anti-inflammatory properties of Ti–OH-MC

First, the free radical scavenging capacities of Ti, Ti–OH, and Ti–OH-MC against 2,2-diphenyl-1-picrylhydrazyl (DPPH) and 2,2'-azino-bis (3-ethylbenzothiazoline-6-sulfonic acid) (ABTS) were evaluated. Briefly, Ti, Ti–OH, and Ti–OH-MC were separately immersed in PBS solution (pH = 6.0) for 24 h to obtain the extracts. The extracts were then added to the DPPH ethanol solution and incubated at 37 °C in the dark for 1 h, as well as to the ABTS solution and incubated at 37 °C for 6 min. The absorbance of each sample was then measured at 517 nm (for DPPH) and 414 nm (for ABTS) using a UV spectrophotometer. The clearance ratio was then calculated using the following Eq. (3):

$$Clearance\ ratio = 1 - \frac{A_t}{A_i} \times 100\% \quad (3)$$

A_i represents the initial absorbance of the DPPH and ABTS solution, and A_t represents the absorbance of the DPPH and ABTS after incubating with the sample.

To further investigate the antioxidant properties, an intracellular antioxidant assay was conducted. L929 cells and RAW 264.7 cells were seeded in 24-well plates at a concentration of 1×10^5 cells per well. After incubation for 24 h, the initial cell culture medium was replaced with DMEM medium containing H_2O_2 (100 μM). At the same time, the Ti, Ti–OH, and Ti–OH-MC samples were individually immersed in the above medium containing H_2O_2. The plates were then incubated at 37 °C for a further 12 h. Cell viability was assessed using the CCK-8 assay, while ROS levels in the cells were detected using the ROS fluorescent probe (DCFH-DA). Images were captured with a fluorescence microscope (ZEISS Axio Observer Z1, Germany). In addition, the efficacy of Ti, Ti–OH, and Ti–OH-MC samples in scavenging intracellular ROS was evaluated using a flow cytometer (Beckman Coulter, USA).

4.8. In vitro macrophage phenotype regulation

The effect of Ti–OH-MC in inducing macrophage polarization was assessed by immunofluorescence staining for the expression of CD206 (M2 surface marker). Briefly, Raw 264.7 cells were seeded at a density of 1×10^5 cells per well in 6-well plates and incubated at 37 °C for 24 h. Subsequently, the cells were stimulated with LPS (100 ng mL^{-1}) for a further 24 h to induce M1 polarization. After that, different samples were immersed in the wells and incubated for another 24 h. The cell culture supernatant was collected, and the levels of the pro-inflammatory cytokines TNF-α and IL-6 and the anti-inflammatory cytokines IL-10 and IL-4, were quantified by enzyme-linked immunosorbent Assay (ELISA). For immunofluorescent staining, macrophages were fixed with 4 % paraformaldehyde, permeabilized with 0.1 % Triton X-100, and blocked with 1 % BSA at room temperature. Rabbit polyclonal antibody against CD206 (dilution: 1:150) was applied followed by Cy3-labeled goat anti-rabbit IgG secondary antibody (dilution: 1:200). Finally, nuclei were stained with DAPI and observed under a fluorescence microscope (ZEISS Axio Observer Z1, Germany). In addition, mRNA-seq analysis was performed to investigate the gene expression profiles of macrophages cultured on different samples. Macrophages (1×10^6) were co-cultured with LPS (100 ng mL^{-1}) for 24 h to induce M1 polarization (M1 group), and then Ti–OH-MC was added to continue the culture for 24 h (Ti–OH-MC group). Each group underwent lysis in Trizol solution followed by mRNA extraction. RNA samples were sequenced by Wuhan Servicebio Technology Co., Ltd., China.

4.9. Properties of Ti–OH-MC in promoting cell adhesion and proliferation

The Ti–OH-MC were immersed in PBS (pH = 6.0) for 3 days and 7 days to obtain Ti–OH-MC-3d and Ti–OH-MC-7d, respectively. Ti, Ti–OH, Ti–OH-MC-3d, and Ti–OH-MC-7d were co-cultured with L929 cells (1×10^5) in the well plate for 24 h. After incubation, the samples were fixed with 4 % paraformaldehyde for 10 min and washed three times (3 min each time) with PBS to remove the residual fixative. To facilitate permeabilization, the samples were treated with 0.1 % Triton X-100 for 5 min and then washed three times with PBS solution. Finally, the cells on the samples were sequentially stained with Actin-Tracker Green working solution (200 μL) before imaging with a fluorescence microscope (ZEISS Axio Observer Z1, Germany). The relative area coverage of fluorescence was measured by Imaje J [42].

4.10. In vivo animal surgery

The New Zealand rabbits, weighing between 2.5 and 3.5 kg, were randomized into three groups (Ti, Ti–OH, and Ti–OH-MC) for gastrointestinal anastomosis. After anesthesia with 3 % sodium pentobarbital (30 mg kg^{-1}), the rabbits were placed in the supine position with their limbs immobilized. First, a midline incision was made in the upper abdomen to explore the abdominal cavity and to identify the sites of preanastomosis: the upper jejunum and the anterior wall of the gastric body. Small incisions were then made in the gastric and intestinal walls, followed by anastomosis using a linear cutting stapler device. Finally, the common opening was closed with a suture technique and the abdominal incision was sutured to close the abdominal cavity.

Rabbits were euthanized on postoperative days 3, 7, and 14, and wound tissue was then collected and fixed with a 4 % formaldehyde solution for subsequent histological analysis and immunofluorescence staining. The inflammation of the anastomotic stoma was assessed by immunohistochemical staining for IL-6, TNF-α, TGF-β, and IL-10. The number of neovascularization was assessed by the level of CD31 expression on day 7. Masson staining was used to assess collagen deposition. Quantification of these stains was performed using Image J software. Furthermore, burst pressure tests of anastomotic stoma were conducted on post-operative days 7 and 14 respectively, to monitor the degree of anastomotic healing. The burst pressure values were recorded when water overflowed from the anastomotic stoma. In addition, the peripheral blood was collected from the rabbits on the day before surgery and on days 3, 7, and 14 postoperatively. The blood was then analyzed using an LH750 automatic blood cell analyzer (Beckman Coulter, USA) to measure white blood cells (WBC), and the centrifuged blood serum was analyzed using an LST008 automated biochemical analyzer (Hitachi, Japan) to determine the levels of ALT, AST, APTT, TT, and FBg.

4.11. Statistical analysis

Results are expressed as mean ± standard deviation (SD) of at least three independent experiments. Statistical analysis was performed using SPSS software (version 26.0 for Windows; SPSS, Chicago, IL, USA). Statistical differences between groups were determined by Student's t-

test or one-way analysis of variance (ANOVA). Significance levels are indicated as $*p < 0.05$, $**p < 0.01$, and $***p < 0.001$.

Ethics approval and consent to participate

This work does not contain results related to human participant.

All animal surgery plans were reviewed and approved by the Animal Ethics Committee of Guangzhou Huateng Biomedical Technology Co., Ltd. All experimental procedures strictly conformed to the Laboratory Animal Care and Use Guidelines.

CRediT authorship contribution statement

Qi Sun: Writing – original draft, Visualization, Validation, Methodology, Formal analysis, Data curation, Conceptualization. **Zifeng Yang:** Writing – review & editing, Writing – original draft, Validation, Project administration, Methodology, Data curation, Conceptualization. **Ruijun Xu:** Writing – original draft, Visualization, Validation, Data curation. **Renjie Li:** Methodology, Data curation. **Yang Li:** Methodology, Data curation. **Feng Wang:** Writing – review & editing, Writing – original draft, Validation, Supervision, Resources, Data curation, Conceptualization. **Yong Li:** Writing – review & editing, Supervision, Resources, Project administration, Funding acquisition, Data curation, Conceptualization.

Declaration of competing interest

The authors declare that they have no known competing financial interests or personal relationships that could have appeared to influence the work reported in this paper.

Acknowledgements

This work was supported by the Leading Innovation Specialist Support Program of Guangdong Province, the National Natural Science Foundation of China (32370836), the National key Clinical Specialty Construction Project (No. 2022YW030009), the GDPH Supporting Fund for Talent Program (KY012021209), the Natural Science Foundation of Guangdong Province (2023A1515110294), the NSFC Incubation Project of Guangdong Provincial People's Hospital (KY0120220049), and the Science and Technology Program of Guangzhou (2023A04J0536).

Appendix A. Supplementary data

Supplementary data to this article can be found online at https://doi.org/10.1016/j.bioactmat.2024.04.021.

References

[1] Y. Chen, M. Chai, C. Xuan, J. Lin, H. Yang, C. Li, M. Xie, S. Ostrovidov, X. Shi, C. Mao, Tuning the properties of surgical polymeric materials for improved soft-tissue wound closure and healing, Prog. Mater. Sci. 143 (2024) 101249, https://doi.org/10.1016/j.pmatsci.2024.101249.

[2] L. Wang, Q. Yang, M. Huo, D. Lu, Y. Gao, Y. Chen, H. Xu, Engineering single-atomic iron-catalyst-integrated 3D-printed bioscaffolds for osteosarcoma destruction with antibacterial and bone defect regeneration bioactivity, Adv. Mater. 33 (2021) 2100150, https://doi.org/10.1002/adma.202100150.

[3] L. Tan, J. Fu, F. Feng, X. Liu, Z. Cui, B. Li, Y. Han, Y. Zheng, K.W.K. Yeung, Z. Li, S. Zhu, Y. Liang, X. Feng, X. Wang, S. Wu, Engineered probiotics biofilm enhances osseointegration via immunoregulation and anti-infection, Sci. Adv. 6 (2020) eaba5723, https://doi.org/10.1126/sciadv.aba5723.

[4] Y. Tang, K. Wang, B. Wu, K. Yao, S. Feng, X. Zhou, L. Xiang, Photoelectrons sequentially regulate antibacterial activity and osseointegration of titanium implants, Adv. Mater. 36 (2024) 2307756, https://doi.org/10.1002/adma.202307756.

[5] J. Fu, W. Zhu, X. Liu, C. Liang, Y. Zheng, Z. Li, Y. Liang, D. Zheng, S. Zhu, Z. Cui, S. Wu, Self-activating anti-infection implant, Nat. Commun. 12 (2021) 6907, https://doi.org/10.1038/s41467-021-27217-4.

[6] I. Mitra, S. Bose, W.S. Dernell, N. Dasgupta, C. Eckstrand, J. Herrick, M. J. Yaszemski, S.B. Goodman, A. Bandyopadhyay, 3D Printing in alloy design to improve biocompatibility in metallic implants, Mater. Today. 45 (2021) 20–34, https://doi.org/10.1016/j.mattod.2020.11.021.

[7] Z. Yuan, J. Wu, Z. Fu, S. Meng, L. Dai, K. Cai, Polydopamine-mediated interfacial functionalization of implants for accelerating infected bone repair through light-activatable antibiosis and carbon monoxide gas regulated macrophage polarization, Adv. Funct. Mater. 32 (2022) 2200374, https://doi.org/10.1002/adfm.202200374.

[8] G. Nandakumar, S.L. Stein, F. Michelassi, Anastomoses of the lower gastrointestinal tract, Nat. Rev. Gastroenterol. Hepatol. 6 (2009) 709–716, https://doi.org/10.1038/nrgastro.2009.185.

[9] A. Lam, B. Fleischer, J. Alverdy, The biology of anastomotic healing—the unknown overwhelms the known, J. Gastrointest. Surg. 24 (2020) 2160–2166, https://doi.org/10.1007/s11605-020-04680-w.

[10] D. Kopelman, O.A. Hatoum, B. Kimmel, L. Monassevitch, Y. Nir, S. Lelcuk, M. Rabau, A. Szold, Compression gastrointestinal anastomosis, Expet Rev. Med. Dev. 4 (2007) 821–828, https://doi.org/10.1586/17434440.4.6.821.

[11] G. Marjanovic, U.T. Hopt, Physiologie der Anastomosenheilung, Chirurg 82 (2011) 41–47, https://doi.org/10.1007/s00104-010-1898-2.

[12] R.B. Morgan, B.D. Shogan, The science of anastomotic healing, Semin. Colon Rectal Surg. 33 (2022) 100879, https://doi.org/10.1016/j.scrs.2022.100879.

[13] E.J. Lee, B.K. Huh, S.N. Kim, J.Y. Lee, C.G. Park, A.G. Mikos, Y.B. Choy, Application of materials as medical devices with localized drug delivery capabilities for enhanced wound repair, Prog. Mater. Sci. 89 (2017) 392–410, https://doi.org/10.1016/j.pmatsci.2017.06.003.

[14] A.K. Gaharwar, I. Singh, A. Khademhosseini, Engineered biomaterials for in situ tissue regeneration, Nat. Rev. Mater. 5 (2020) 686–705, https://doi.org/10.1038/s41578-020-0209-x.

[15] C.R. Arciola, D. Campoccia, L. Montanaro, Implant infections: adhesion, biofilm formation and immune evasion, Nat. Rev. Microbiol. 16 (2018) 397–409, https://doi.org/10.1038/s41579-018-0019-y.

[16] C. Chen, G. Chu, W. He, Y. Liu, K. Dai, J. Valdez, A. Moores, P. Huang, Z. Wang, J. Jin, M. Guan, W. Jiang, Y. Mai, D. Ma, Y. Wang, Y. Zhou, A janus Au–polymersome heterostructure with near-field enhancement effect for implant-associated infection phototherapy, Adv. Mater. 35 (2023) 2207950, https://doi.org/10.1002/adma.202207950.

[17] C. Ding, R. He, T. Cheng, J. Wang, X. Liu, G. Guo, Y. Chen, Bacterial outer membrane-based biomimetic immune adaptors: mild immunomodulatory and bacterial targeted delivery strategy against implant-related infections, Adv. Funct. Mater. 33 (2023) 2304168, https://doi.org/10.1002/adfm.202304168.

[18] G. Chu, M. Guan, J. Jin, Y. Luo, Z. Luo, T. Shi, T. Liu, C. Zhang, Y. Wang, Mechanochemically reprogrammed interface orchestrates neutrophil bactericidal activity and apoptosis for preventing implant-associated infection, Adv. Mater. (2024) 2311855, https://doi.org/10.1002/adma.202311855.

[19] L. Bai, P. Chen, Y. Zhao, R. Hang, X. Yao, B. Tang, C. Liu, Y. Xiao, R. Hang, A micro/nano-biomimetic coating on titanium orchestrates osteo/angio-genesis and osteoimmunomodulation for advanced osseointegration, Biomaterials 278 (2021) 121162, https://doi.org/10.1016/j.biomaterials.2021.121162.

[20] Y. Zhao, L. Bai, Y. Zhang, R. Yao, Y. Sun, R. Hang, X. Chen, H. Wang, X. Yao, Y. Xiao, R. Hang, Type I collagen decorated nanoporous network on titanium implant surface promotes osseointegration through mediating immunomodulation, angiogenesis, and osteogenesis, Biomaterials 288 (2022) 121684, https://doi.org/10.1016/j.biomaterials.2022.121684.

[21] G. Xiang, K. Liu, T. Wang, X. Hu, J. Wang, Z. Gao, W. Lei, Y. Feng, T.H. Tao, In situ regulation of macrophage polarization to enhance osseointegration under diabetic conditions using injectable silk/sitagliptin gel scaffolds, Adv. Sci. 8 (2021) 2002328, https://doi.org/10.1002/advs.202002328.

[22] F. Zhang, Q. Hu, Y. Wei, W. Meng, R. Wang, J. Liu, Y. Nie, R. Luo, Y. Wang, B. Shen, Surface modification of titanium implants by pH-Responsive coating designed for Self-Adaptive antibacterial and promoted osseointegration, Chem. Eng. J. 435 (2022) 134802, https://doi.org/10.1016/j.cej.2022.134802.

[23] S. Wu, J. Xu, L. Zou, S. Luo, R. Yao, B. Zheng, G. Liang, D. Wu, Y. Li, Long-lasting renewable antibacterial porous polymeric coatings enable titanium biomaterials to prevent and treat peri-implant infection, Nat. Commun. 12 (2021) 3303, https://doi.org/10.1038/s41467-021-23069-0.

[24] Y.-G. Chen, C.-X. Li, Y. Zhang, Y.-D. Qi, X.-H. Liu, J. Feng, X.-Z. Zhang, Hybrid suture coating for dual-staged control over antibacterial actions to match well wound healing progression, Mater. Horiz. 9 (2022) 2824–2834, https://doi.org/10.1039/D2MH00591C.

[25] Y. Zhao, L. Xu, F. Kong, L. Yu, Design and preparation of poly(tannic acid) nanoparticles with intrinsic fluorescence: a sensitive detector of picric acid, Chem. Eng. J. 416 (2021) 129090, https://doi.org/10.1016/j.cej.2021.129090.

[26] Y. Zhang, J. Cao, M. Lu, Y. Shao, K. Jiang, X. Yang, X. Xiong, S. Wang, C. Chu, F. Xue, Y. Ye, J. Bai, A biodegradable magnesium surgical staple for colonic anastomosis: in vitro and in vivo evaluation, Bioact. Mater. 22 (2023) 225–238, https://doi.org/10.1016/j.bioactmat.2022.09.023.

[27] L. Song, M. Gao, L. Tan, Z. Ma, P. Ni, M. Zhou, D. Na, Application potential of Mg–Zn–Nd alloy as a gastrointestinal anastomosis nail material, Acta Metall. Sin. 35 (2022) 609–620, https://doi.org/10.1007/s40195-021-01296-0.

[28] D. Li, J. Li, S. Wang, Q. Wang, W. Teng, Dually crosslinked copper-poly(tannic acid) nanoparticles with microenvironment-responsiveness for infected wound treatment, Adv. Healthcare Mater. 12 (2023) 2203063, https://doi.org/10.1002/adhm.202203063.

[29] A. Bandyopadhyay, I. Mitra, S.B. Goodman, M. Kumar, S. Bose, Improving biocompatibility for next generation of metallic implants, Prog. Mater. Sci. 133 (2023) 101053, https://doi.org/10.1016/j.pmatsci.2022.101053.

[30] X. Qi, E. Cai, Y. Xiang, C. Zhang, X. Ge, J. Wang, Y. Lan, H. Xu, R. Hu, J. Shen, An immunomodulatory hydrogel by hyperthermia-assisted self-cascade glucose depletion and ROS scavenging for diabetic foot ulcer wound therapeutics, Adv. Mater. 35 (2023) 2306632, https://doi.org/10.1002/adma.202306632.
[31] A.K. Farha, Q.-Q. Yang, G. Kim, H.-B. Li, F. Zhu, H.-Y. Liu, R.-Y. Gan, H. Corke, Tannins as an alternative to antibiotics, Food Biosci. 38 (2020) 100751, https://doi.org/10.1016/j.fbio.2020.100751.
[32] J. Park, T.Y. Kim, Y. Kim, S. An, K.S. Kim, M. Kang, S.A. Kim, J. Kim, J. Lee, S. Cho, J. Seo, A mechanically resilient and tissue-conformable hydrogel with hemostatic and antibacterial capabilities for wound Care, Adv. Sci. 10 (2023) 2303651, https://doi.org/10.1002/advs.202303651.
[33] S.A. Eming, T.A. Wynn, P. Martin, Inflammation and metabolism in tissue repair and regeneration, Science 356 (2017) 1026–1030, https://doi.org/10.1126/science.aam7928.
[34] Y. Guo, S. Ding, C. Shang, C. Zhang, M. Li, Q. Zhang, L. Gu, B.C. Heng, S. Zhang, F. Mei, Y. Huang, X. Zhang, M. Xu, J. Jiang, S. Guo, X. Deng, L. Chen, Multifunctional PtCuTe nanosheets with strong ROS scavenging and ROS-independent antibacterial properties promote diabetic wound healing, Adv. Mater. 36 (2024) 2306292, https://doi.org/10.1002/adma.202306292.
[35] Z. Song, H. Yu, L. Hou, Y. Dong, M. Hu, P. Wei, W. Wang, D. Qian, S. Cao, Z. Zheng, Z. Xu, B. Zhao, Y. Huang, W. Jing, X. Zhang, Mechanics-resilient HA/SIS-based composite scaffolds with ROS-scavenging and bacteria-resistant capacity to address infected bone regeneration, Adv. Funct. Mater. (2024) 2315382, https://doi.org/10.1002/adfm.202315382.
[36] S.A. Eming, P.J. Murray, E.J. Pearce, Metabolic orchestration of the wound healing response, Cell Metabol. 33 (2021) 1726–1743, https://doi.org/10.1016/j.cmet.2021.07.017.
[37] B. Zhou, W. Lin, Y. Long, Y. Yang, H. Zhang, K. Wu, Q. Chu, Notch signaling pathway: architecture, disease, and therapeutics, Signal Transduct. Targeted Ther. 7 (2022) 95, https://doi.org/10.1038/s41392-022-00934-y.
[38] W. Chen, Y. Shao, X. Li, G. Zhao, J. Fu, Nanotopographical surfaces for stem cell fate control: engineering mechanobiology from the bottom, Nano Today 9 (2014) 759–784, https://doi.org/10.1016/j.nantod.2014.12.002.
[39] Y. Li, Y. Xiao, C. Liu, The horizon of materiobiology: a perspective on material-guided cell behaviors and tissue engineering, Chem. Rev. 117 (2017) 4376–4421, https://doi.org/10.1021/acs.chemrev.6b00654.
[40] J. Pelipenko, P. Kocbek, B. Govedarica, R. Rošic, S. Baumgartner, J. Kristl, The topography of electrospun nanofibers and its impact on the growth and mobility of keratinocytes, Eur. J. Pharm. Biopharm. 84 (2013) 401–411, https://doi.org/10.1016/j.ejpb.2012.09.009.
[41] M.C. Bottino, V. Thomas, G.M. Janowski, A novel spatially designed and functionally graded electrospun membrane for periodontal regeneration, Acta Biomater. 7 (2011) 216–224, https://doi.org/10.1016/j.actbio.2010.08.019.
[42] J. Schindelin, I. Arganda-Carreras, E. Frise, V. Kaynig, M. Longair, T. Pietzsch, S. Preibisch, C. Rueden, S. Saalfeld, B. Schmid, J.-Y. Tinevez, D.J. White, V. Hartenstein, K. Eliceiri, P. Tomancak, A. Cardona, Fiji: an open-source platform for biological-image analysis, Nat. Methods 9 (2012) 676–682, https://doi.org/10.1038/nmeth.2019.